ADVANCED MATERIALS
www.advmat.de

Ultrathin, Transferred Layers of Silicon Oxynitrides as Tunable Biofluid Barriers for Bioresorbable Electronic Systems

Ziying Hu, Jie Zhao, Hexia Guo, Rui Li, Mingzheng Wu, Jiahong Shen, Yue Wang, Zheng Qiao, Yue Xu, Greg Haugstad, Dongqi An, Zhaoqian Xie, Irawati Kandela, Khizar R. Nandoliya, Yu Chen, Yi Yu, Qunyao Yuan, Junyu Hou, Yujun Deng, Abdulaziz H. AlDubayan, Quansan Yang, Liangsong Zeng, Di Lu, Jahyun Koo, Wubin Bai, Enming Song, Shenglian Yao, Chris Wolverton,* Yonggang Huang,* and John A. Rogers**

Bio/ecoresorbable electronic systems create unique opportunities in implantable medical devices that serve a need over a finite time period and then disappear naturally to eliminate the need for extraction surgeries. A critical challenge in the development of this type of technology is in materials that can serve as thin, stable barriers to surrounding ground water or biofluids, yet ultimately dissolve completely to benign end products. This paper describes a class of inorganic material (silicon oxynitride, SiON) that can be formed in thin films by plasma-enhanced chemical vapor deposition for this purpose. In vitro studies suggest that SiON and its dissolution products are biocompatible, indicating the potential for its use in implantable devices. A facile process to fabricate flexible, wafer-scale multilayer films bypasses limitations associated with the mechanical fragility of inorganic thin films. Systematic computational, analytical, and experimental studies highlight the essential materials aspects. Demonstrations in wireless light-emitting diodes both in vitro and in vivo illustrate the practical use of these materials strategies. The ability to select degradation rates and water permeability through fine tuning of chemical compositions and thicknesses provides the opportunity to obtain a range of functional lifetimes to meet different application requirements.

1. Introduction

The rapid proliferation of electronics with lifetimes that significantly exceed their actual periods of use leads to the creation of millions of tons of solid electronic waste each year, with associated management challenges. Physically "transient" electronics, constructed using materials that are water soluble to environmentally benign end products, addresses this problem through disappearance in natural environments as part of a disposal process that imposes minimal impact.[1–5] Related types of transient electronic devices can also serve as medical implants for sensing, monitoring, stimulating, and providing other forms of functionality over an operating period that matches to a biological process such as wound healing.[6–9] Afterward, the devices disappear naturally in the body without a trace, to eliminate the need for extraction surgeries. Recent research highlights

Z. Hu, H. Guo, M. Wu, Y. Wang, D. Lu, J. Koo, W. Bai, S. Yao, J. A. Rogers
Querrey-Simpson Institute for Bioelectronics
Northwestern University
Evanston, IL 60208, USA
E-mail: jrogers@northwestern.edu

J. Zhao, Q. Yuan, J. Hou
State Key Laboratory of Molecular Engineering of Polymers
Department of Materials Science
Fudan University
Shanghai 200433, China
E-mail: jiezhao@fudan.edu.cn

The ORCID identification number(s) for the author(s) of this article can be found under https://doi.org/10.1002/adma.202307782

DOI: 10.1002/adma.202307782

H. Guo, J. Shen, Z. Qiao, A. H. AlDubayan, C. Wolverton, J. A. Rogers
Department of Materials Science and Engineering
Northwestern University
Evanston, IL 60208, USA
E-mail: c-wolverton@northwestern.edu

R. Li, D. An, Z. Xie
State Key Laboratory of Structural Analysis
Optimization and CAE Software for Industrial Equipment
Department of Engineering Mechanics
and International Research Center for Computational Mechanics
Dalian University of Technology
Dalian 116024, P. R. China

Y. Wang, Y. Xu, J. A. Rogers
Department of Biomedical Engineering
Northwestern University
Evanston, IL 60208, USA

a range of transient materials options in metals (Mg, Zn, Mo, Fe, and W), inorganic semiconductors and dielectrics (Si, SiO_2, and oxides of some biodegradable metals), and polymer substrates and coatings (poly(lactic-*co*-glycolic acid) (PLGA), polycaprolactone, etc.).[10–12] A remaining challenge is in the development of encapsulating materials as water barriers for applications that demand stable operation for timescales ranging from a few days to a few weeks. Polymer thin films commonly used in packaging materials, especially in the food industry, can offer some utility but their water permeability and tendency to swell upon exposure to water represent severe disadvantages for applications in transient electronics.[13,14] These challenges are particularly pronounced when such materials are used as thin films with micrometer-scale thicknesses, where specific values for water permeability range from 10^2 to 10^0 (g m^{-2}) day^{-1}.[15] Natural wax materials can serve effectively as hydrophobic encapsulation layers that maintain performance of underlying devices for up to two weeks in phosphate buffer solution (PBS; pH = 7.4) at 37 °C.[16] Further studies are required, however, to improve the flexibility of natural wax without compromising its barrier properties. In addition, given the complex composition of natural wax materials, the degradation rates, and mechanisms are still unclear.[16,17] Our previous studies show that polyanhydride-based biodegradable polymers have the ability to sustain operation of underlying biodegradable electronic systems for durations between a few hours to a week while fully immersed in aqueous solutions that approximate physiological conditions.[18] Matching the operating times of biodegradable electronic systems with those of slow (weeks) biological processes such as wound healing requires, however, encapsulation materials with improved water barrier properties.

Inorganic materials provide attractive alternatives. Monocrystalline, device-grade silicon in ultrathin forms (i.e., micro/nanomembranes) can dissolve at various rates in different types of biofluids as well as in seawater and other naturally occurring forms of water.[19,20] The main dissolution product, silicic acid, is biocompatible and environmentally benign at the low levels of concentration created by silicon in micro/nanomembrane form.[21,22] A key limitation of this approach is that the micro/nanomembranes typically derive from silicon on insulator wafers that are expensive and difficult to scale to large areas. Silicon oxides (SiO_x) and silicon nitrides(SiN_x) formed by plasma-enhanced chemical vapor deposition (PECVD) represent additional options,[23,24] but published reports suggest that thin films of such materials provide effective barrier function only for several days in ambient conditions. Data captured from organic light-emitting diode encapsulated with these materials indicate that pinholes are a primary cause of leakage of gases or liquids. Moreover, these pinholes can also lead to low fracture toughness and poor electrical insulation.[25] Dense films of silicon dioxide grown by thermal processes on silicon wafers offer the necessary performance to serve as long-lived barriers to biofluids, with stable operation across timescales that approach 70 years even for films with sub-micrometer thicknesses.[26] A disadvantage is that the rates for dissolution are too slow (0.04 nm day^{-1} at 37 °C) for most envisioned applications in transient electronics. Also, thermally grown SiO_2 permits diffusion and accumulation of some species of ions in biofluids, with negative effects on the properties of many types of electronic devices.[26] These circumstances motivate the development of alternative inorganic thin-film materials.

Here, we introduce a class of biodegradable inorganic material (silicon oxynitride, SiON) formed by PECVD with controlled compositions in thin films that can serve as stable biofluid barriers for timescales as long as months. As with silicon micro/nanomembranes and the PECVD materials described above, the main dissolution product is silicic acid, which is biocompatible.[23] Facile routes to flexible, large-area, transparent trilayer assemblies yield encapsulating structures with good mechanical toughness. Demonstrations in wireless LEDs devices both in vitro and in vivo illustrate the practical use of these trilayer encapsulating materials in transient electronics. Furthermore, the composition of the SiON can be fine-tuned to achieve desired dissolution rates and water barrier properties, aligned with required operating times for biodegradable electronic systems in nerve regeneration (≈2 weeks)[27] and bone healing (1–2 months).[28,29] The optical transparency of these materials creates additional opportunities in bioresorbable optoelectronics, with potential for use in implantable optogenetic devices.[30]

G. Haugstad
Characterization Facility
University of Minnesota
100 Union St. SE, Minneapolis, MN 55455, USA
I. Kandela
Center for Developmental Therapeutics
Northwestern University
Evanston, IL 60208, USA
I. Kandela
Chemistry Life Processes Institute
Northwestern University
Evanston, IL 60208, USA
K. R. Nandoliya
Department of Neurological Surgery
Northwestern University Feinberg School of Medicine
Chicago, IL 60611, USA
Y. Chen, Y. Yu
School of Physical Science and Technology
Shanghai Tech University
Shanghai 201210, China
Y. Deng
State Key Laboratory of Mechanical System and Vibration
Shanghai Jiao Tong University
Shanghai 200240, China
Q. Yang, L. Zeng, Y. Huang, J. A. Rogers
Department of Mechanical Engineering
Northwestern University
Evanston, IL 60208, USA
E-mail: y-huang@northwestern.edu
E. Song
Institute of Optoelectronics
Fudan University
Shanghai 200433, P. R. China
J. A. Rogers
Department of Chemistry
Department of Neurological Surgery
and Department of Electrical Engineering and Computer Science
Northwestern University
Evanston, IL 60208, USA

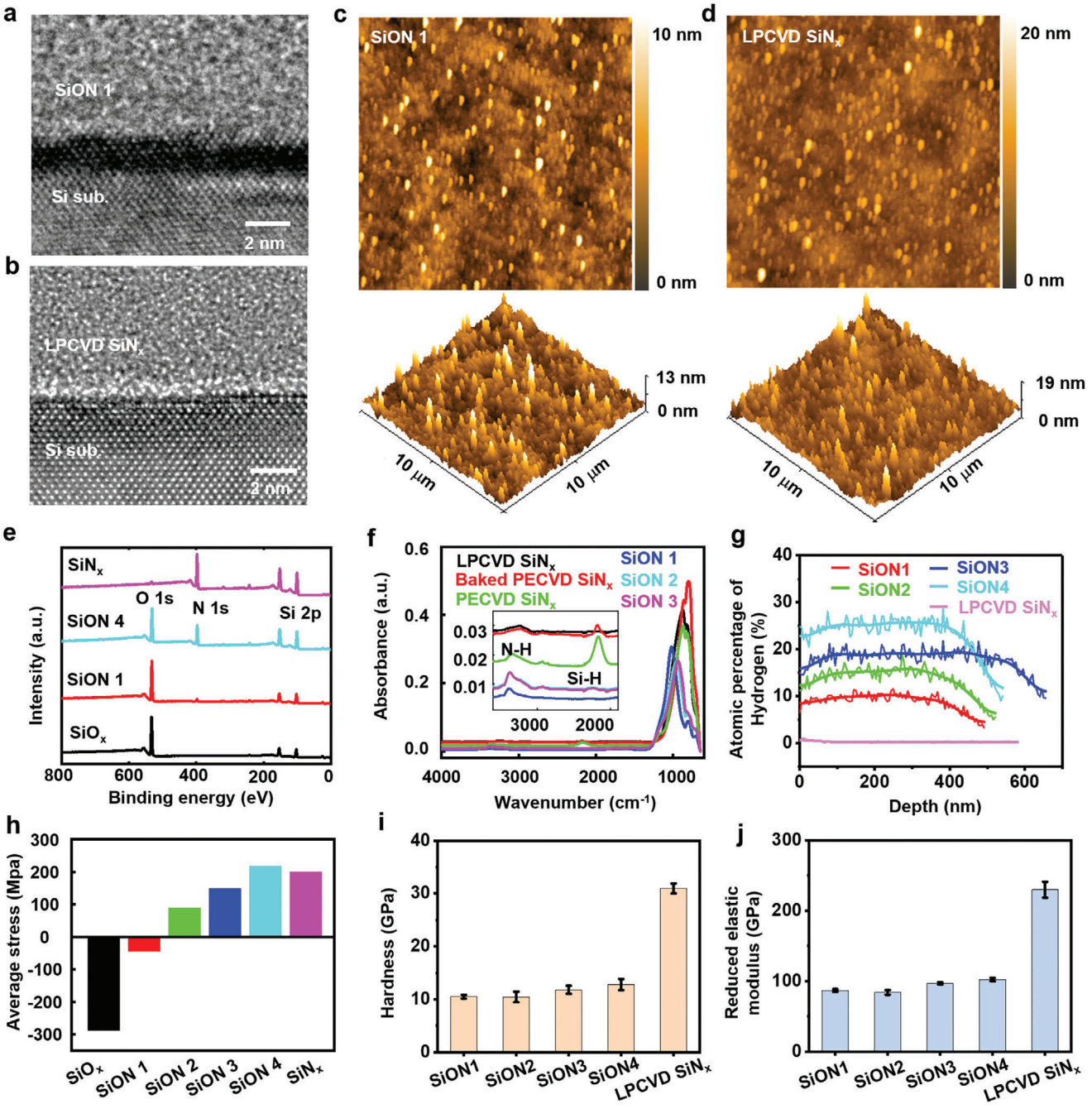

Figure 1. Properties of PECVD SiO_xN_y thin films. a) Cross-sectional TEM images of SiON 1 on a Si wafer (Si sub.). b) Cross-sectional TEM images of LPCVD SiN_x films. c) 2D and 3D AFM images of SiON 1. Surface roughness: Ra = 0.79 nm. d) 2D and 3D AFM images of LPCVD SiN_x. Surface roughness: Ra = 1.06 nm. Scanning area: 10 μm × 10 μm. e) XPS analysis of different PECVD thin films. f) FTIR of LPCVD SiN_x, PECVD SiN_x, PECVD SiN_x baked at 800 °C, and different SiON films. Inset shows the H bond of different films. g) Depth profiles of the hydrogen distribution in SiON 1–4 and LPCVD SiN_x films on Si wafers. The thicknesses of SiON 1–4 and LPCVD SiN_x films are 490 nm (red line), 520 nm (green line), 655 nm (blue line), 540 nm (cyan line), and 580 nm (light magenta line), respectively. The atomic percentages of hydrogen in SiON 1–4 and LPCVD SiN_x films are 10.3%, 15.8%, 19.3%, 25.7%, and 0.3%, respectively. Thin lines are experimental data and bold lines are fitting results using the Fourier transform smoothing function of a commercial software package (Origin). h) Average stresses for different PECVD thin films grown on Si wafers. i) Hardness of SiON 1–4 and LPCVD SiN_x films. j) Reduced elastic modulus of SiON 1–4 and LPCVD SiN_x films. The film thickness of SiON 1–4 and LPCVD SiN_x ranges from 520 to 655 nm. (i,j) Results are presented as mean ± standard deviation ($n \geq 4$).

2. Results and Discussions

2.1. Fabrication and Characterization of PECVD SiO_xN_y

Figure 1a,b shows the morphologies of PECVD SiON 1 and low-pressure chemical vapor deposition (LPCVD) SiN_x thin films characterized using transmission electron microscopy (TEM). The images indicate that both SiON 1 and LPCVD SiN_x have amorphous structures and that LPCVD SiN_x is denser than SiON 1. 2D and 3D atomic force microscope images reveal the surface roughness of SiON 1–4 and LPCVD SiN_x films, as shown in Figure 1c,d and Figure S1 (Supporting Information). The results indicate that the surfaces of films of SiN_x deposited by LPCVD (average surface roughness, Ra = 1.06 nm, Figure 1d) is slightly rougher than those of SiON films formed by PECVD (Figure 1c; Figure S1 Supporting Information: SiON 1, Ra = 0.79 nm; SiON 2, Ra = 0.64 nm; SiON 3, Ra = 0.75 nm; SiON 4, Ra = 0.69 nm). Comparisons of the properties and performance characteristics of silicon oxide, nitride, and oxynitride thin films formed on Si wafers via PECVD appear in **Table 1**.

The compositions of these materials follow from the proportion of the reacting gases, including SiH_4, N_2O, and NH_3 (Table S1, Supporting Information). X-ray photoelectron spectroscopy (XPS) reveals the relative presence of oxides, nitrides, and oxynitrides (Figure 1e). SiO_xN_y films synthesized from recipe 1 to 4 show a nitrogen content that ranges from 6.54% to 29.4% (Table 1). Fourier-transform infrared spectroscopy (FTIR) reveals the surface chemical properties (Figure 1f) in terms of the amount of hydrogen bonds (N—H and Si—H) in LPCVD SiN_x, PECVD SiN_x, and PECVD SiON. The findings correlate with the completeness of the reaction with ammonia. Suppression of the Si—H peak in films of SiN_x formed by LPCVD follows from the slow and complete reaction of the source gases at high temperatures (800 °C). From SiON 1 to SiON 4, the increased growth rates also lead to increases in the amount of hydrogen bonds (N—H) in the films. The hydrogen concentration in SiON 1–4 and LPCVD SiN_x films as a function of film thickness, as in Figure 1g, show that the atomic percentages of hydrogen in SiON 1–4 and LPCVD SiN_x films are 10.3%, 15.8%, 19.3%, 25.7%, and 0.3%, respectively, measured using elastic recoil detection (ERD).[31] From SiON 1 to SiON 4 with increasing N (the N_2O flow increases in fabrication conditions), the atomic percentage of hydrogen increases, while films of LPCVD SiN_x show negligible hydrogen. The FTIR spectra and ERD results confirm that PECVD SiON films are hydrogenated, i.e., SiON:H, which reacts with water molecules, and that the distribution of hydrogen is uniform throughout the film. These surface hydrogen bonds have a strong effect on the rate of hydrolysis reactions.

The average residual stresses for films of PECVD SiO_x, SiON 1, SiON 2, SiON 3, SiON 4, and SiN_x on Si wafers are −288, −45, 90, 150, 218, and 208 MPa, respectively (Figure 1h). As an intermediate phase between oxides and nitrides, SiON can be formed with a range of residual stresses, densities, and refractive indices by controlling the relative proportions of the reaction gases and the ratio of high and low frequency radio frequency power used during the deposition process (Table S2, Supporting Information). Figure 1i,j presents the hardness and reduced elastic modulus of SiON 1–4 and LPCVD SiN_x, respectively, based on the load–displacement curves (Figure S2, Supporting Information) of films characterized using nanoindentation.[32] The hardness and modulus of LPCVD SiN_x are 30.9 ± 0.9 and 229.6 ± 11.3 GPa, respectively. The hardness of SiON 1–4 films is 10.5 ± 0.3, 10.4 ± 0.9, 11.8 ± 0.8, and 12.8 ± 1.1 GPa, and the modulus of SiON 1–4 films is 86.8 ± 1.9, 84.0 ± 3.3, 96.8 ± 1.6, 102.2 ± 2.4 GPa, respectively, both showing an increase with an increase of N content. These values and the observed trends of hardness and modulus that increase with film refractive index (Table 1) are in good agreement with previous reports.[33]

In vitro studies with human cortical neuron cell lines (HCN-2) serve as initial evaluations of the biocompatibility of these materials. Experiments involve placing disk-shaped samples of LPCVD SiN_x, PECVD SiN_x, and PECVD SiON thin films grown on silicon wafers into the wells of a 96-well plate with a density of 20 000 cells per well. After incubating neuron cells with these films for 48 h, cell viability results show no significant differences ($P = 0.240$, Kruskal–Wallis test, GraphPad Prism). These results confirm the cell-level biocompatibility of these silicon-based inorganic thin films (Figure S3, Supporting Information). The chronic effects of film degradation (4 weeks) in the context of uses in implants are revealed in the following in vivo biocompatibility studies.

2.2. Measurements of Dissolution Kinetics in PBS

Measurements in phosphate-buffed saline (PBS, pH = 7.4) at five temperatures (T, **Figure 2a**: 25 °C; Figure 2b: 37 °C; Figure 2c: 70 °C; Figure 2d: 80 °C; Figure 2e: 96 °C) define the dissolution rates of SiO_xN_y films with various compositions, from recipe 1 to 4 (Table S1, Supporting Information). The rates for the four SiO_xN_y films and their dependence on T appear in Figure 2f, consistent with an exponential dependence on 1/T as expected based on an Arrhenius scaling relationship: $k = Ae^{-\frac{E_a}{k_B T}}$, where A is the pre-exponential factor, E_a is the activation energy, and k_B is the Boltzmann constant. The calculated activation energies lie within a range (0.71, 0.77, 0.77, 0.70 eV for SiON 1–4) consistent with silica (0.48–1.11 eV)[26] and with silicon nitrides (0.54–1.14 eV)[34,35] in deionized water or other aqueous media such as solutions of NaCl. The measured average dissolution rates at 37 °C are 7.5, 10.1, 12.2, and 21.3 nm day^{-1} for SiON 1 to 4, respectively, which are much higher than those of previously reported inorganic barrier materials, such as thermally grown silicon oxide (≈0.04 nm day^{-1})[26] and LPCVD SiN_x (≈0.3 nm day^{-1}).[36] Reflectometry defines the thicknesses of the SiO_xN_y films during the dissolution tests. Cross-sectional scanning electron microscope (SEM) images illustrate the decrease in thickness, as in Figure 2g (0, 5, and 10 h for SiON 4, 80 °C PBS). Measurements of average dissolution rates in deionized water and Dulbecco's modified Eagle medium (DMEM, a commonly used growth medium for cells) at 96 °C are in Figure S4 of the Supporting Information. The rate increases from SiON 1 to SiON 4 (see details in Figure S4, Supporting Information), consistent with trends observed in PBS. Furthermore, the results of dissolution of SiON 1 formed with different residual stress values through control over the growth conditions, also measured at 96 °C, are in Figure S5 of the Supporting Information, with other related details in Table S2 of the

Table 1. Composition, mass density, and refractive index of PECVD SiON 1–4 and LPCVD SiN_x.

Items		Atomic percentage [%]			Mass density [g cm^{-3}]	Refractive index at 633 nm
		Si	O	N		
PECVD	SiO_x	37.0	63.0	0	1.52	1.47
$SiH_4 + N_2O \rightarrow SiO_x (+H_2 + N_2)$						
$SiH_4 + NH_3 \rightarrow SiN_x (+H_2)$						
$SiH_4 + N_2O + NH_3 \rightarrow SiO_xN_y (+H_2 + N_2)$						
	SiON 1	39.2	54.3	6.5	2.23	1.52
	SiON 2	40.2	47.4	12.4	2.34	1.56
	SiON 3	41	39.2	19.8	2.38	1.60
	SiON 4	41.9	28.7	29.4	2.43	1.67
	SiN_x	53.8	2.4	43.8	2.70	2.13
LPCVD	SiN_x	51	0.2	48.8	3.10	2.19

Supporting Information. The dissolution rates show no significant dependence on stress.

Figure S6 of the Supporting Information summarizes the parameters of a theoretical model of reactive diffusion for these dissolution processes. Since the initial thicknesses are much smaller than the in-plane dimensions, a 1D treatment can capture the behaviors. Figure S6a of the Supporting Information illustrates a single layer model of a thin film barrier with an initial thickness h_{Barrier} in PBS solution (see details in the Supporting Information). Figure S6b–f of the Supporting Information sequentially presents theoretical (lines) and measured (dots) changes in thickness of different barriers in PBS solution at various temperatures, i.e., 25, 37, 70, 80, and 96 °C. The theoretically predicted dissolution rates of SiON 1–4 versus temperature (Figure S7a, lines, Supporting Information) agree with the measurements (dots). Figure S7b of the Supporting Information shows the lifetimes of SiON 1–4 at 37 °C, indicating an approximately linear dependence on the initial thickness. The previously described experiments and simulation results identify that diffusion through the SiON is negligible and that the hydrolysis process is the essential cause of eventual failure.

2.3. Density-Functional Theory (DFT) Simulation of Amorphous PECVD SiON

Results of DFT simulation provide some insights into the stability of PECVD SiON with different compositions. The amorphous structures can be simulated by relatively small supercells based on the special quasirandom structure (SQS) method. Ground state SiO_2 (space group *I-42d*) serves as the initial structure and some oxygen atoms were substituted by nitrogen and silicon atoms to achieve the composition ratios of different SiO_xN_y. Two sets of SQS structures with 48 atoms and 96 atoms are constructed where SiON 1 to SiON 4 were represented by $Si_{19}N_3O_{26}$, $Si_{19}N_6O_{23}$, $Si_{19}N_9O_{20}$, and $Si_{20}N_{14}O_{14}$, respectively. For SQS structure, configurational entropy is calculated by

$$S = k_B \left(x\ln(x) + (1-x)\ln(1-x)\right) \quad (1)$$

where k_B is the Boltzmann constant and x is the partial occupancy on a substitution site. The convex hull method is used to study the thermal stability of different SiO_xN_y. In one phase space, the convex hull is defined as a linear combination of the most stable (i.e., the lowest energy) phases at each composition. Thus, the convex hull distance, which also means the stability of a compound can be defined as

$$\Delta H_{\text{stability}} = \Delta H_f - \Delta H_{\text{hull}} \quad (2)$$

where $\Delta H_{\text{stablility}}$ is the stability (convex hull distance), ΔH_{hull} is the convex hull energy at that composition without the given compound and ΔH_f is the formation enthalpy of that compound, which is defined as

$$\Delta H_f = E_{SiO_xN_y} - \mu_{Si} - x\mu_O - y\mu_N \quad (3)$$

where $E_{SiO_xN_y}$ is the total energy of SiO_xN_y compound, μ_{Si}, μ_O, and μ_N are the chemical potentials of silicon, oxygen, and nitrogen, respectively. The magnitude of $\Delta H_{\text{stability}}$ can, therefore, indicate the thermal stability of a given compound, where a smaller convex hull distance means a compound is more stable. DFT calculations are performed to determine the intrinsic properties of different SiO_xN_y. The simulated structures with 96 atoms are shown in **Figure** 3a. The stabilities of four structures are in the order of SiON 1, SiON 2, SiON 3, and SiON 4, where SiON 1 is the most stable one (Figure 3b). To determine the dissolution rate of SiO_xN_y in H_2O, the Gibbs reaction energy is computed for each structure based on

$$\Delta G_{\text{react}} = \Delta H_{SiO_xN_y} + a\Delta H_{H_2O} - b\Delta H_{SiO_2} - c\Delta H_{NH_3} - d\Delta H_{H_2} \quad (4)$$

where ΔH is the formation energy of each compound, and coefficients are determined by the balanced chemical reaction equations. The Gibbs reaction energy at $T = 0$ K (Figure 3c) demonstrates that the reaction of SiON 4 with H_2O is the easiest one to happen, which agrees with its largest dissolution rate among the four structures. Given the randomness of the sites in SQS structures, the configurational entropy should be considered, which can lower the free energy of the compound at finite temperature

$$\Delta H(T) = \Delta H_f - TS_{\text{config}} \quad (5)$$

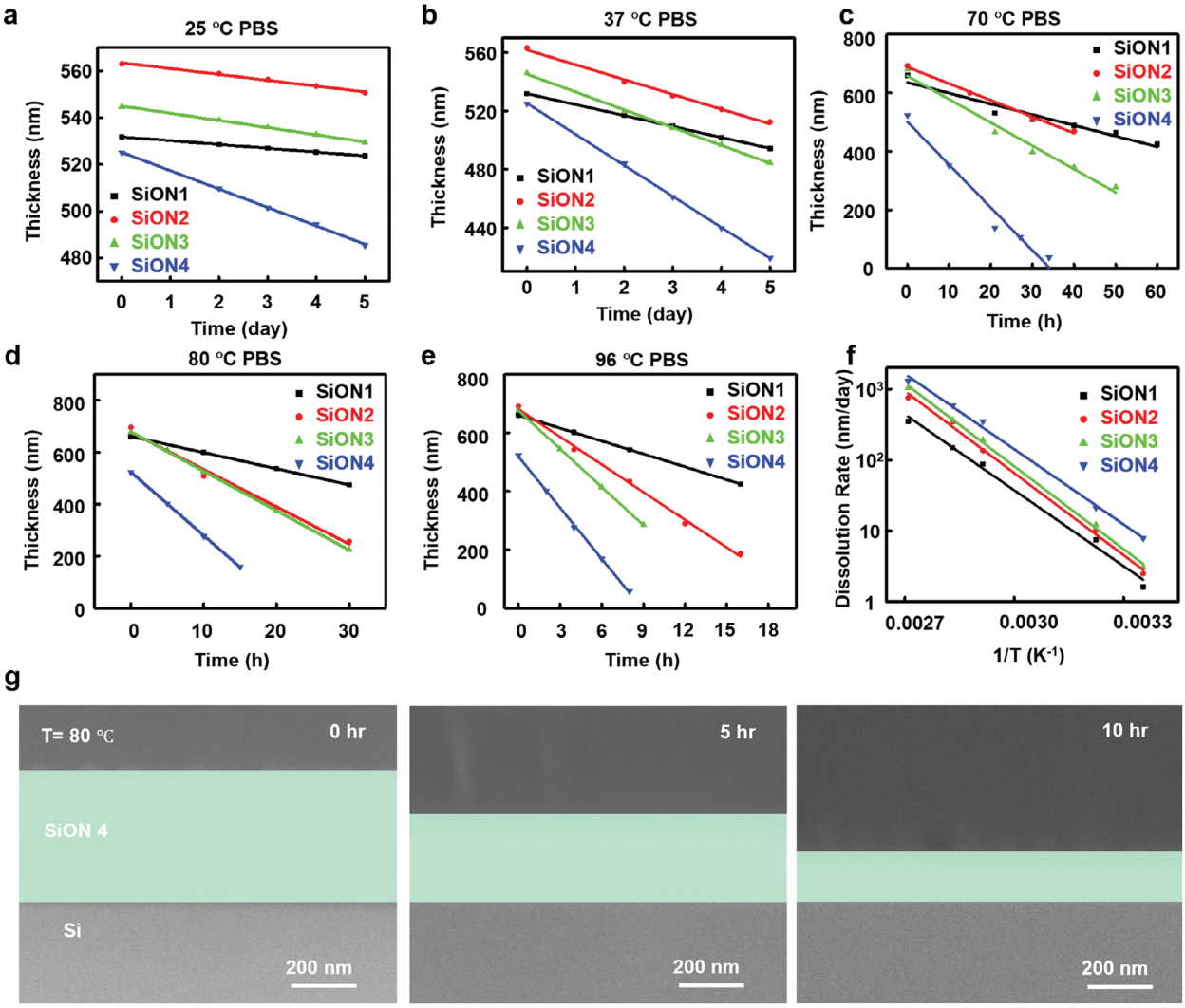

Figure 2. Dissolution kinetics of SiO_xN_y barrier layers. a–e) The change in thickness and dissolution rate calculated from linear fitting of results of soaking samples of SiON 1–4 in the PBS solution at various temperatures, a) 25 °C, SiON 1: 1.6 nm day^{-1}, SiON 2: 2.5 nm day^{-1}, SiON 3: 3.1 nm day^{-1}, SiON 4: 7.9 nm day^{-1}. b) 37 °C, SiON 1: 7.5 nm day^{-1}, SiON 2: 10.1 nm day^{-1}, SiON 3: 12.2 nm day^{-1}, SiON 4: 21.3 nm day^{-1}. c) 70 °C, SiON 1: 88.1 nm day^{-1}, SiON 2: 135.6 nm day^{-1}, SiON 3: 191.0 nm day^{-1}, SiON 4: 351.0 nm day^{-1}. d) 80 °C, SiON 1: 149.6 nm day^{-1}, SiON 2: 344.9 nm day^{-1}, SiON 3: 364.8 nm day^{-1}, SiON 4: 586.5 nm day^{-1}. e) 96 °C, SiON 1: 353.3 nm day^{-1}, SiON 2: 757.2 nm day^{-1}, SiON 3: 1045.1 nm day^{-1}, SiON 4: 1398.6 nm day^{-1}. f) The dissolution rates (derived from (a)–(e)) plotted on a log scale as a function of temperature for SiON 1–4 suggest an exponential relationship with 1/*T* (K). g) Cross-sectional SEM images showing decreases in the thickness of SiON 4 thin film in PBS at 80 °C after 5 and 10 h.

where S_{config} is configurational entropy calculated using Equation (1) and ΔH_f is the ground state formation energy given as Equation (3). Figure 3d shows that the Gibbs reaction energy trends for four SiO_xN_y are consistent over the entire temperature range. DFT calculations indicate the intrinsic differences of these four types of SiO_xN_y. Under the actual conditions, the stability of SiON is also affected by the amount of hydrogen bonds, residue stress, and pinhole densities of the thin films.

2.4. Biofluid Barrier Properties

Patterns of thin films of magnesium (Mg) allow visualization and quantification of the water penetration behaviors of overlying films under test conditions that involve immersion in PBS. Here, serpentine structures Mg films deposited by electron-beam evaporation (e-beam, thickness = 300 nm) react with water that passes through barrier layers coated or transferred on top, according to $Mg + 2H_2O \rightarrow Mg(OH)_2 + H_2$, leading to changes in resistance and visible signatures observable by optical microscopy (**Figure 4a**). Results obtained from PECVD SiN_x (thickness: 2 μm) indicate almost immediate failure (<1 day) after soaking in PBS (Figure 4b). By contrast, SiN_x with the same thickness formed by LPCVD leads to negligible changes in resistance for more than two months. LPCVD SiN_x exhibits a lower amount of dangling bonds compared with PECVD SiN_x due to the slow and complete reaction at elevated deposition temperatures as shown in Figure 1f. Moreover, the mass densities

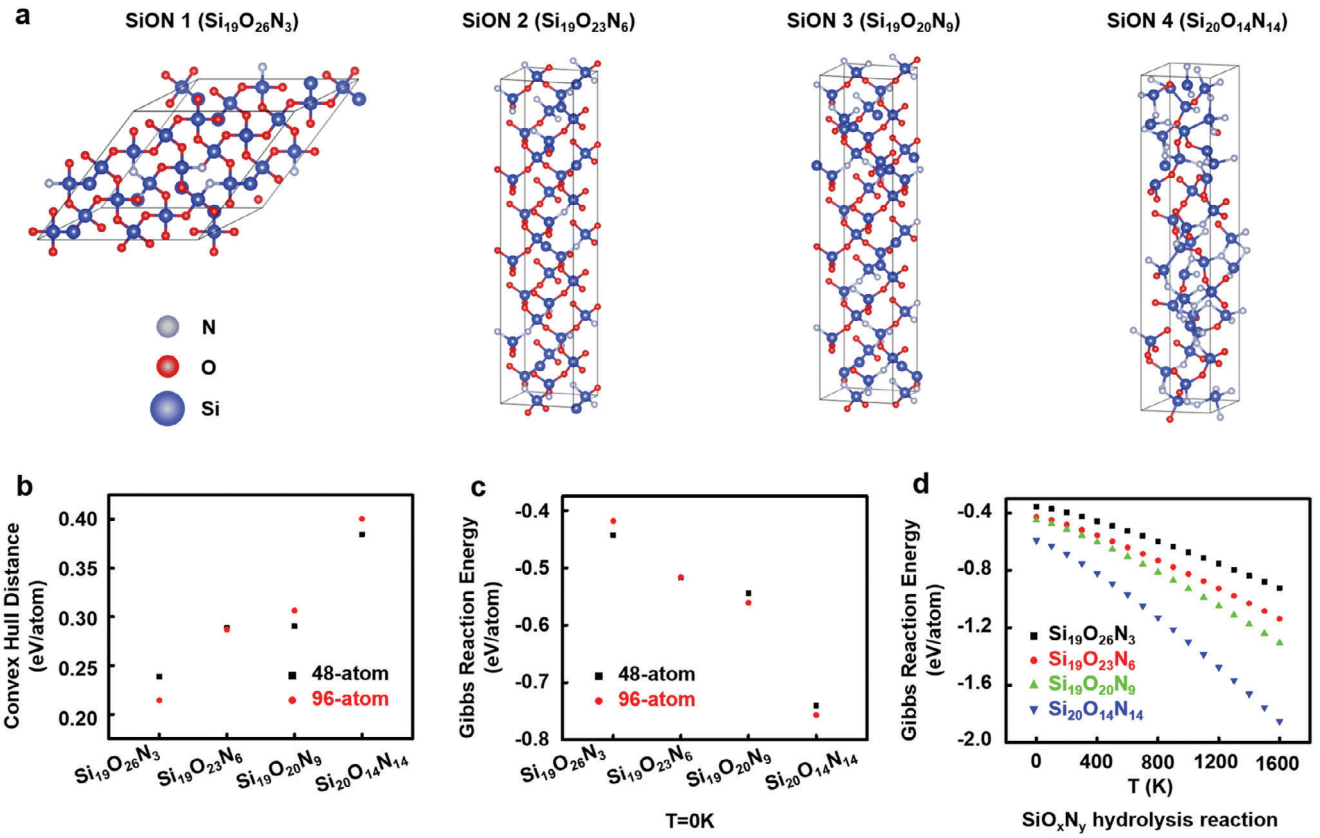

Figure 3. DFT computations of the intrinsic stability of various SiO_xN_y. a) Simulated structure with 96 atoms of SiON 1–4 based on special quasirandom structures. b) Evaluation of the stability of each SiO_xN_y by the convex hull distance method. c) Simulated Gibbs reaction energy of the hydrolysis reaction of each SiO_xN_y at 0 K. d) Simulated Gibbs reaction energy of the hydrolysis reaction of each SiO_xN_y at finite temperature.

are 3.1 g cm^{-3} for LPCVD SiN_x and 2.5 g cm^{-3} for PECVD SiN_x (Table 1). The results suggest that LPCVD SiN_x exhibits enhanced barrier properties partly due to its high atomic density and low amount of hydrogen bonds. Both PECVD SiON 1 and SiON 2 (thickness: 6 μm) can protect the Mg serpentine for more than two months, comparable to LPCVD SiN_x (thickness: 2 μm). A bilayer model is established to further examine the barrier properties of various thin films as illustrated in Figure S8a of the Supporting Information. Figure S8b of the Supporting Information shows the theoretically predicted resistance changes of 300-nm-thick Mg protected by different barriers as a function of immersion time in PBS solution at 37 °C, illustrating good agreement between theoretical (lines) and measured results (dots).

The series of optical images of the serpentine traces of Mg in Figure 4c reveals the major pathway for liquid or vapor water permeation through the SiON films. In Figure 4c, the PECVD SiON 1 protects the Mg traces for at least 50 days during the soak test at 37 °C. The image at 70 days shows reactions of Mg, visible as dark areas that follow from leakage of water through local defects. The corrosion of Mg then proceeds along the trace as shown in the image at 90 days. These images demonstrate that water permeates the SiON film via local pinholes, consistent with previous reports,[23,26,37,38] but that this permeation proceeds over much longer timeframes compared to those with PECVD SiO_x and SiN_x (film thickness: 1 μm, barrier lifetime: less than 1 day at 37 °C).[26]

2.5. Fabrication and Utilization of the Trilayer Encapsulation Structure

Figure 5a summarizes the steps for forming centimeter-scale SiON-based trilayer stacks designed to improve the mechanical robustness of the isolated inorganic films. The procedure begins with the growth of a protection layer of SiN_x (≈1 μm, not shown) followed by SiON on a Si wafer by PECVD. Next, SiN_x deposition continues with PECVD to cover the SiON film and four edges (≈1 cm width) of the backside of the Si wafer. The SiN_x acts as an etching mask during immersion in 25 wt% tetramethylammonium hydroxide (TMAH) solution at 85 °C for 12–16 h to eliminate silicon from the unprotected backside of the wafer. Reactive ion etching (RIE) then removes the mask to leave a thin film of SiON supported by the Si frame. Drop-casting PLGA (≈10 μm) on both sides of the SiON and laser cutting the Si frame yields a freestanding trilayer structure of PLGA/SiON/PLGA. Figure 5b shows photographs of various stages of this process. This packaging strategy can be easily scaled to sizes limited only by the dimensions of the wafer (current maximum size: ≈450 mm diameter). The inorganic layer is at the neutral

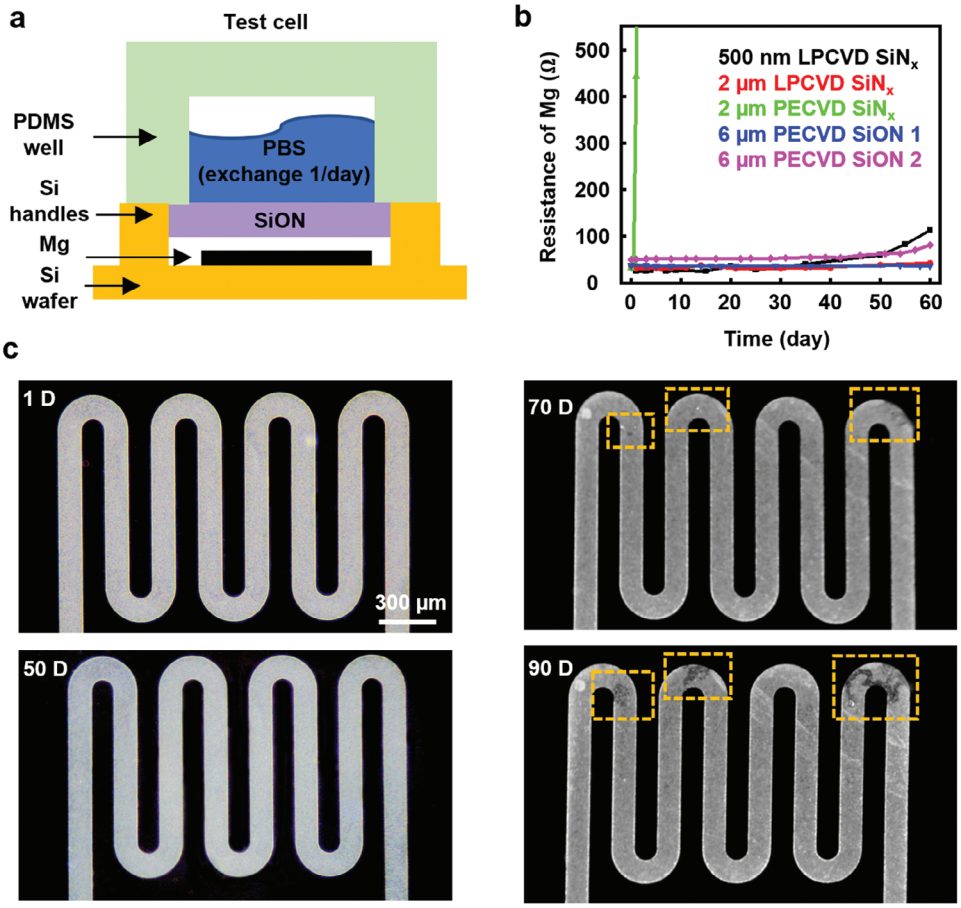

Figure 4. Biofluid barrier properties of various thin inorganic films. a) Experimental setup with a thin patterned structure of Mg allows direct imaging of the penetration of water through an overlying thin inorganic film barrier layer. b) Plot of the resistance of a serpentine structure of Mg encapsulated with different thin inorganic films as a function of time of immersion in PBS solution. Black and red dots represent the experimental data points of 500-nm and 2-μm-thick LPCVD SiN_x thin films, respectively. Green, blue, and magenta dots are the experimental data points of 2-μm-thick PECVD SiN_x, 6-μm-thick SiON 1, and 6-μm-thick SiON 2, respectively. c) Optical images of a serpentine structure encapsulated with a film of SiON 1 (thickness: 6 μm) at various times at 37 °C.

mechanical plane thereby enabling good flexibility and robust mechanical properties.[39] For a thin film of PECVD SiON under pure bending, the minimum curvature radius R_{min} can be predicted by the following equation

$$R_{min} = \frac{t}{2\epsilon_f} \quad (6)$$

where t is the film thickness and ϵ_f is the material fracture strain. Assuming that the fracture strain of PECVD SiON is ≈1%,[40] the bending radius of a 2-μm-thick SiON thin film can be as small as 0.1 mm. Finite element analysis/method and theoretical modeling reveal aspects associated with the processibility of these trilayer structures shown in Figures S9 and S10 of the Supporting Information. The strain of the inorganic barrier material wrapped by PLGA is computed when fixed at one end and subjected to gravity (9.8 m s^{-2}). As shown in Figure S9c of the Supporting Information, the maximum strain in the 2-μm-thick inorganic layer of the trilayer film located at the neutral axis of deformation decreases by up to 85% as the thickness of the PLGA layer increases from 6 to 20 μm. The minimum bending radius depends on the thickness of the SiON layer (Figure S10a,b, Supporting Information), instead of the thickness of the PLGA layer (Figure S10a,c, Supporting Information). The minimum bending radius of trilayer films with 6 μm SiON and 20 μm PLGA is 0.28 mm.

Figure 5c,d provides examples of these trilayer (top: 20 μm PLGA/6 μm SiON1/20 μm PLGA, bottom: 20 μm PLGA/2 μm LPCVD SiN_x/20 μm PLGA) structures as encapsulation for biodegradable wireless electronics, with an ability to operate in a stable fashion over extended periods in aqueous environments at 37 °C. The device here consists of a radio frequency (RF) energy harvester (two 50-μm-thick Mo foils spaced with a 10-μm-thick PLGA dielectric layer), designed to provide wireless power to a light-emitting diode (LED). By heating to 70 °C for 15 min, the PLGA layers partially melt to allow bonding of two trilayer structures on top and bottom of the device. Application of biodegradable polyanhydride materials reported previously[17] at the perimeter edges limit leakage through this path. The same strategy is applied to the trilayer LPCVD SiN_x encapsulation

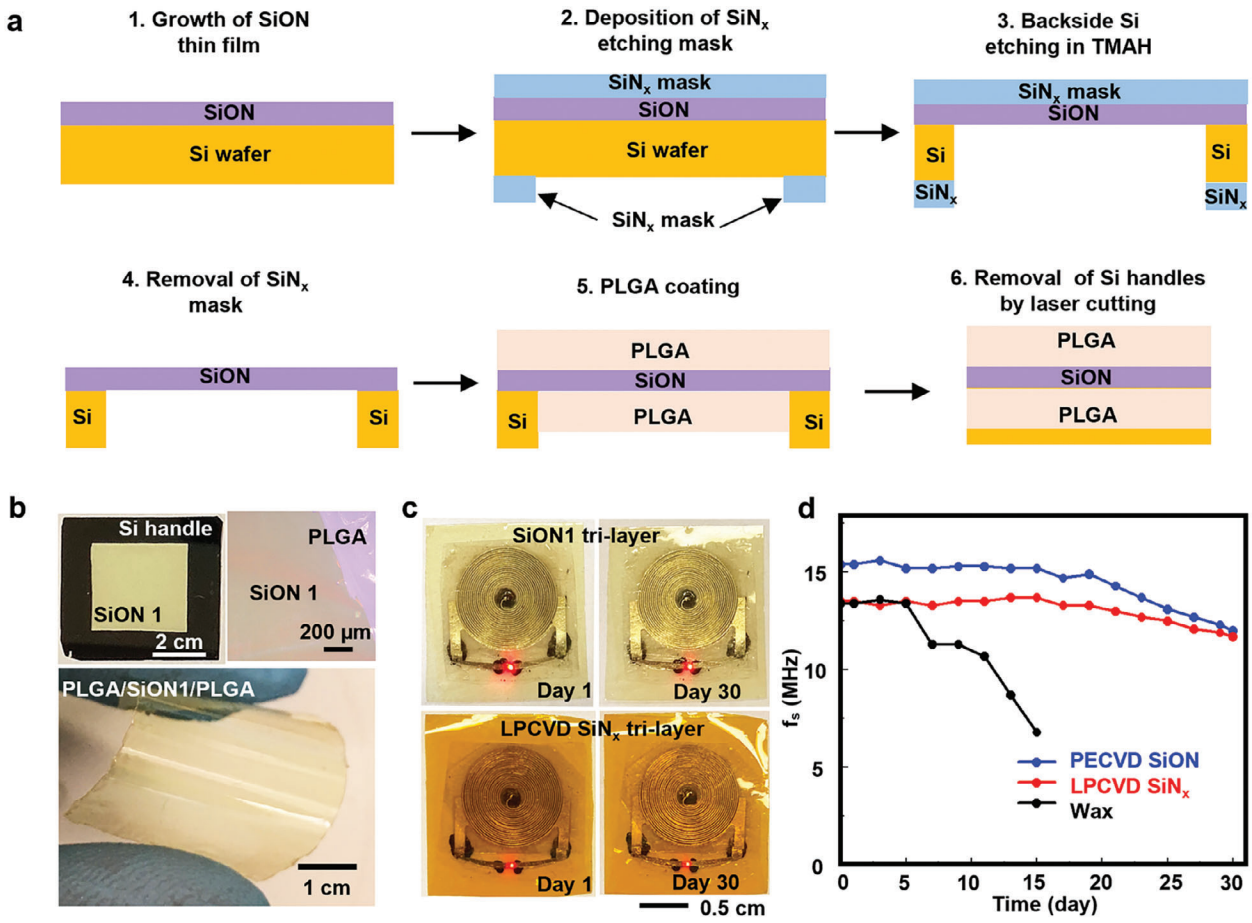

Figure 5. Biofluid barrier properties of packaging structures that combine inorganic thin films and organic polymers. a) Schematic illustrations of the key steps for forming trilayer encapsulation structures. b) Optical images of a SiON 1 film with Si handle structures (upper left), SiON 1 coated on a film of PLGA (upper right) and a photograph of trilayer PLGA/SiON 1/PLGA encapsulation material (bottom, 20 µm PLGA/6 µm SiON 1/20 µm PLGA). c) Photographs of wireless devices encapsulated by trilayer PECVD SiON 1 (top, 20 µm PLGA/6 µm SiON 1/20 µm PLGA) and trilayer LPCVD SiN_x (bottom, 20 µm PLGA/2 µm LPCVD SiN_x/20 µm PLGA) materials and soaked in PBS (pH 7.4, 37 °C) for 1 day and 30 days, respectively. d) Plot of the resonance frequencies of wireless devices sealed using different encapsulation materials with the associated photographs shown in (c) as a function of time of immersion in PBS solution.

materials. Compared with candelilla wax, PECVD SiON and LPCVD SiN_x thin films in these trilayer configurations significantly extend the operation lifetimes in PBS at body temperature (Figure 5d). Compared with LPCVD SiN_x trilayer structures, SiON-based trilayer structures have improved transparency for various optical bioelectronics applications. The slight change in the resonance frequency during soaking likely follows from water that permeates from the edges, thereby revealing a potential area for improvement.

2.6. Biocompatibility and Biodegradation of the Trilayer Encapsulation Structure

Figures 6a and S11 (Supporting Information) present cross-sectional SEM images and photographs of SiON 1 films and the trilayer (PLGA/SiON 1/PLGA) encapsulation film before implantation and after implantation in mice for 4 weeks. The thicknesses of SiON 1 and PLGA are 6.62 ± 0.03 and 12.1 ± 0.9 µm, respectively, before implantation. The thickness of SiON 1 films decreases to 6.44 ± 0.08 µm after implantation in mice for 4 weeks. The average degradation rate of SiON 1 in mice is 6.28 nm day^{-1}, which is close to that obtained from the benchtop testing, i.e., 7.5 nm day^{-1}, in PBS at 37 °C. The weight of the mice and their key organs in the implanted and control groups are nearly identical (Figure 6b). The distribution of Si in these organs measured by inductively coupled plasma optical emission spectrometry also shows that the degradation of SiON 1 films does not cause Si accumulation in any organ (Figure 6c). Complete blood count (CBC) and blood chemistry provide additional indicators for organ-related responses. CBC demonstrates the average level of red blood cells, hemoglobin, hematocrit, platelets, and white blood cells (Figure 6d). Analysis of blood chemistry includes the level of blood urea nitrogen, proteins, glucose, and liver enzyme (Figure 6e). Both tests show no significant differences between the implanted group and the control mice. Histological analysis of the skin and muscles in the implantation region indicates no signs of inflammation in the surrounding skin and muscles

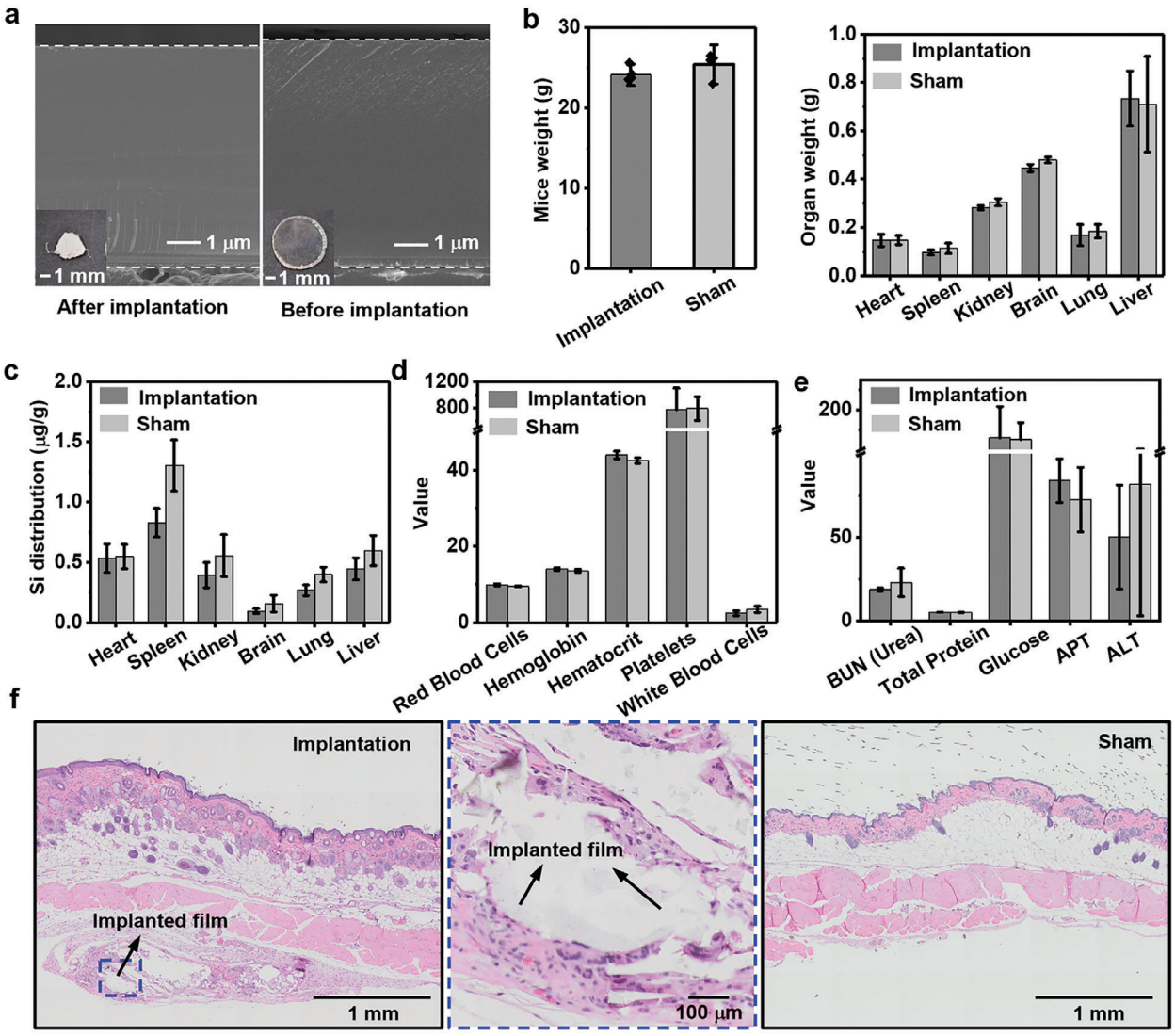

Figure 6. In vivo studies of biocompatibility and biodegradation of trilayer films (PLGA/SiON 1/PLGA) in mouse models. a) Cross-sectional SEM images of SiON 1 after (left) and before (right) implantation in mice for 4 weeks. Insets are photographs of trilayer films after and before implantation in mice for 4 weeks. b) Weight of mice (left) and key organs (right) with/without implanted films. Five mice with implanted films represent the implantation group and four mice without implanted films represent the sham group. Four pieces of trilayer film (diameter: 5 mm) were implanted in each mouse under the skin in the implantation group. c) Silicon distribution in heart, spleen, kidney, brain, lung, and liver, in the implantation and sham groups. d) Complete blood count analysis on mice. e) Blood chemistry analysis on mice. f) Histological analysis of mice skin with/without film implantation. Results in (b)–(e) are presented as mean ± standard deviation ($n \geq 3$).

(Figure 6f; Figure S12a,b, Supporting Information). The thickness differences of the skin, including dermis and hypodermis, between the implanted group and the control mice are not significant (Figure S12c,d, Supporting Information), consistent with good biocompatibility of the trilayer films.

2.7. In Vivo Studies on the Water Barrier Performance of the Trilayer Encapsulation Structure

To further evaluate the water barrier performance of the trilayer encapsulation structure, **Figure** 7a,b presents wireless LED devices, adapted from the designs described previously, with encapsulation using the trilayer structure (diameter: 10 mm) undergoing subcutaneous implantation in mice ($n = 3$). Devices with encapsulation are functional after implantation in mice for at least 18 days, as indicated by the illuminated LEDs that are wirelessly powered by a near-field communication (NFC) expansion board (Figure S13, Supporting Information). Devices lacking the trilayer encapsulation structure (Figure 7c), serving as a control group ($n = 3$), fail to operate after implantation in mice for only 2 days. Figure 7d,e shows the reflection coefficient (S11) of the device with and without encapsulation as a function of frequency, respectively. The peak frequency of devices with the trilayer encapsulation structure remains stable in mice for 18 days and shows a slight shift upon implantation for 21 days. The value

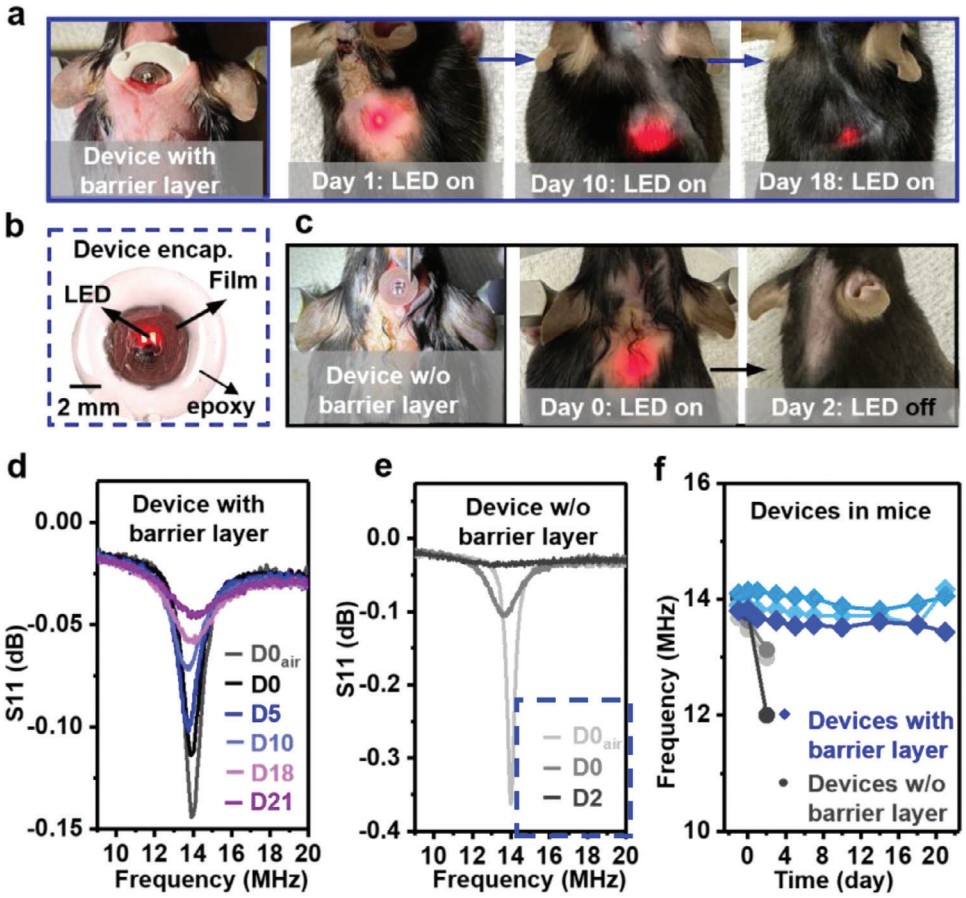

Figure 7. In vivo studies of the water barrier performance of the trilayer encapsulation structure (PLGA/SiON 1/PLGA). a) Wireless LED devices encapsulated using trilayer films implanted in mice ($n = 3$). LEDs of all devices can be wirelessly powered after implantation for at least 18 days using an NFC expansion board. b) A photograph of LED devices with encapsulation using trilayer films. Diameter of a device after encapsulation: 10 mm. c) LED devices lacking trilayer film encapsulation in mice ($n = 3$). LEDs fail to be illuminated in 2 days after implantation. d) Changes of S11 of a representative wireless device encapsulated using trilayer films in mice for 21 days. e) Changes of S11 of a representative wireless device without encapsulation implanted in mice for 2 days. f) The resonance frequency with and without encapsulation shown in (a) and (c) as a function of the implantation period. (d,e) Data labeled as "$D0_{air}$" were acquired before device implantation and other data points were obtained after implantation.

of the peak frequency decreases gradually, which is likely due to the change of the medium between the device and the transmitter coil (diameter: 10 mm) because of the recovery of the skin as well as water absorption of the outer PLGA layer of the trilayer structure. By contrast, the peak frequency for devices without the trilayer structure shows a significant decrease and an obvious shift. Figure 7f presents frequency changes over the implantation period for three devices with encapsulation and three devices without encapsulation. These results prove the effective water barrier performance of trilayer structure in mice.

3. Conclusion

In conclusion, this report introduces PECVD SiON thin films as biodegradable encapsulation materials for transient electronics. In vivo studies suggest that SiON and its dissolution products are biocompatible, indicating the potential for its use in temporary biomedical devices as well as in environmentally degradable systems. Moreover, large area, flexible organic/inorganic trilayer structures can serve as encapsulating materials that are mechanical robust for reliable device integration. Demonstrations of these ideas in wireless LED devices both in vitro and in vivo illustrate the practical use in a representative type of transient electronic device. The ability to select degradation rates and water permeability by choice of chemical compositions and thicknesses provides the opportunity to obtain a range of functional lifetimes to meet different application requirements.

4. Experimental Section

Film Growth: LPCVD SiN_x was deposited with a Tystar LPCVD low-stress nitride furnace. The growth conditions for gas flow, pressure, and temperature are summarized in Table S1 of the Supporting Information with a deposition rate of ≈3.2 nm min^{-1}. The standby temperature was 550 °C and ramp rate was 10 °C min^{-1}. PECVD deposition was performed with an STS LpX CVD apparatus. The growth parameters for gas flow, pressure, plate temperature, high/low frequency generator power for various compositions are summarized in Table S1 of the Supporting Information.

Morphology and Surface Roughness Characterization: Morphologies/structures and surface roughnesses of inorganic thin films deposited on Si wafers formed using different deposition techniques were

characterized with TEM (JEM-F200, JEOL) and atomic force microscopy (AFM; Dimension Edge, Bruker), respectively. The specimens for TEM characterization were prepared using Multi Beam System (JIB-4700F JEOL) equipped with liquid gallium ion source. A protective layer of carbon (thickness: 1–2 µm) was coated on the thin film selectively before ion beam etching. A lamella was formed and thinned to 120 nm in thickness under a voltage of 30 kV and milled to less than 100 nm in thickness by using a voltage of 5 kV with a current of 10 pA.

Film Composition Characterization: X-Ray Photoelectron Spectroscopy: The elemental percentages of the resulting films were characterized using XPS (ESCALAB 250Xi, Thermo Fisher Scientific) after in situ etching of the films for 120 s (several nanometers in depth).

FTIR Characterization: The FTIR spectra of various inorganic thin films grown on Si wafers were acquired with a Nicolet iS50 spectrometer (Thermo Nicolet) in attenuated reflection mode from 650 to 4000 cm^{-1} to characterize the surface properties. The characteristic absorption peak of Si–H or N–H is ≈2100 and 3400 cm^{-1}.

Rutherford Backscattering Spectrometry (RBS) and ERD: RBS and ERD (for hydrogen content) were simultaneously performed using an MAS 1700 pelletron tandem ion accelerator (5SDH, National Electrostatics Corporation, NEC: Middleton, WI) to generate a 3.05 MeV He^{++} beam with a current of ≈30 nA measured at the (electrically floating) sample. He^{++} ions (i.e., alpha particles) that backscatter by nuclear collisions (RBS), and target H nuclei that forward recoil from collisions with the alphas, were counted by Ortec silicon ion detectors that were positioned at scattering angles of 165° and 30° with respect to the incident beam, respectively; the latter detector was blocked by a 12 µm layer foil to stop all incoming particles heavier than hydrogen. Visibly luminescent control samples were employed to locate the beam position per sample goniometer coordinates and sample tilt. The beam was 2 × 2 mm (square) in cross-section, but the sample was tilted by 75° (to enable ERD geometry) thereby elongating the analytical spot to ≈8 mm along the one (horizontal) dimension. Two spectra consisting of counts versus data channel (≈3.25 keV per channel) of backscattered He^{++} and forward recoiled H^{+} (with energetics described by classical billiard ball kinematics) were simultaneously acquired on each sample with a multichannel analyzer controlled by NEC RC43 software. The total integrated incident charge was $Q \approx 40$ µC per spectrum (which together with detector solid angle determines the absolute number of counted particles).

To approximately quantify H content, including its depth dependence, the ERD spectra were normalized to that of (cleaved) muscovite mica as a standard (9.5 at%) as follows. First, the spectra on mica were collected to triple the particle integration (then divided by three in counts) as that employed on the samples of interest, so as to produce a less noisy signal for normalization purposes. Second, the mica counts per data channel were gained up by ≈15% to account for the larger stopping power on mica, per comparative spectral simulations (using the freeware QUARK) of a slab of mica and a same-thickness slab of the samples of interest (the latter composition being determined from XPS results). Third, the counts for two of the five ERD spectra of interest were gained up by ≈10% to account for small discrepancies in charge integration, as determined from the RBS signal at the low energy portion of the spectra (substrate signal). The approximate calibration of the horizontal axis (from data channels to depth) of the processed spectra of interest used the measured thickness of the thickest sample of interest.

Film Stress Measurement: The thin film stress was measured with a stylus profilometer (Veeco Dektak) by performing a line scan before and after thin film deposition. A 4 in. Si wafer substrate was aligned on the stage and a line scan (scan length: 1000 µm, stylus force: 3 mg, profile: Hills & Valleys) was performed and saved as baseline. After deposition, the film thickness was measured by a reflectometer (Filmetrics F20). A postdeposition line scan was executed with the wafer placed at the same location and the same parameters. The stress was calculated via Analysis/Compute Stress module in the software (Dektak) after loading the baseline and postdeposition scan data files and inputting the film thickness.

Film Hardness and Modulus Measurement: The hardness and modulus of thin films were measured by applying and removing a load to a film in a highly controlled manner with a displacement of 40 nm (displacement-control mode) using quasistatic nanoindentation (Hysitron TI 950 TriboIndenter, Bruker). The loading/unloading speed was set to 5 nm s^{-1} and the probe was held for 2 s at maximum displacement. The values of hardness and modulus were extracted from the unloading portion of load–displacement curves using the Oliver–Pharr model in the data analysis package of the nanoindenter.

Dissolution Test: The inorganic film under test was immersed into PBS solution (or DI H_2O, DMEM) under ambient conditions (25 °C) or in an oven at a given temperature (37, 70, 80, and 96 °C) to measure the dissolution rate of various SiON compositions at different temperatures. The film thicknesses were measured by a reflectometer (Filmetrics F20) nondestructively. Cross-sectional SEM images can also yield the film thicknesses in a destructive manner.

Evaluation of Biofluid Barrier Property with Mg Serpentine Traces: Photolithography with AZ5214E was performed with a maskless aligner (Heidelberg MLA150) to define the serpentine-shaped patterns. Mg deposition with an AJA e-beam evaporator followed by removal of photoresist AZ5214 defined the Mg serpentine traces (thickness: ≈300 nm). To measure the resistances of Mg serpentine traces during dissolution tests, the Mg was connected to Au leads by depositing a layer of Au (thickness: ≈100 nm) at the ends of the traces. An inorganic film was then placed onto the Mg serpentines with the edges sealed by a marine epoxy (Loctite). A PDMS well held PBS solution on top of the test unit and the entire setup was placed in an oven at 37 °C. The resistances and optical images of the Mg serpentines were monitored daily.

Preparation of Trilayer Packaging Materials: The procedure began with the growth of SiON films on Si wafers by PECVD. PECVD SiN_x covered the SiON film and edges of the backside of the Si wafer, which served as the etching mask for the subsequent chemical etching process. The samples were immersed in 25 wt% TMAH solution at 85 °C for 12–16 h to eliminate the uncovered backside of the wafer. RIE then removed the etching mask residues and yielded the SiON thin film supported by Si handles. Drop-casting PLGA on both sides of the SiON thin film and laser cutting the Si handles after drying enabled the formation of trilayer PLGA/SiON/PLGA encapsulation materials.

Fabrication of Bioresorbable Devices Encapsulated by Trilayer Materials: The bioresorbable device here consisted of an RF energy harvester, which included two Mo coils (thickness: ≈50 µm) stacked on top of one another and spaced with an ≈10 µm thick PLGA dielectric layer. The energy harvester provided wireless power to a commercial LED. A UV laser cutter (LPKF, ProtoLaser U4) defined the coil structure by selectively removing Mo. Conductive wax electrically connected all components of the device. Two pieces of trilayer materials bonded above and below the device by heating to 70 °C for 15 min sealed the system. To minimize leakage issues at the edges during the PBS soaking test, biodegradable polyanhydrides were utilized to cover the entire wireless device. The resonant frequency was recorded by network analyzer (Keysight, N9923A).

Fabrication of Wireless LED Devices for In Vivo Demonstration of Trilayer Materials: Wireless LED devices adapted from the designs described previously for in vitro tests served as the basis for in vivo evaluations. These devices consisted of an RF energy harvester based on two Cu coils (diameter: 6 mm, 10 turns; thickness: 18 µm) stacked on top of one another and spaced with a polyimide dielectric layer (thickness: 75 µm). The fabrication process used steps similar to those for the in vitro test devices. A UV laser cutter defined the coil structure by selectively removing Cu. Low-temperature indium solder electrically connected all components of the device, including two LEDs, two diodes, and one capacitor. The energy harvester provided wireless power to a commercial LED via an NFC extension board (STMicroelectronics), operating at 13.56 MHz (Figure S13, Supporting Information). The resonant frequency of devices was measured using a vector network analyzer.

To evaluate the water barrier performance of trilayer materials in mice, three devices were encapsulated using the materials. The encapsulation process included placing a device on a circular cover glass (thickness ≈ 150 µm) and sealing the device with a circular trilayer film (diameter: 10 mm, thickness ≈ 40 µm) by slightly heating them to 65 °C for a few

minutes. Applying epoxy to seal film edges further prevented water permeation from those edges.

Biocompatibility and In Vivo Biodegradation: All procedures associated with the animal studies followed the Guide for the Care and Use of Laboratory Animals of the National Institutes of Health and approved by The Institutional Animal Care and Use Committee at Northwestern University.

Female mice (C57/BL6; age at the initiation of the treatment: 8–12 weeks; Charles River Laboratories) were anaesthetized using isoflurane gas (1–2% isoflurane in oxygen) in an anesthetizing chamber during the implantation surgery. The films under test were trilayer PLGA/SiON 1/PLGA films cut into a circular shape (diameter: 5 mm, thickness ≈ 30 µm). After sterilizing by UV irradiation overnight, four films were implanted in the dorsal subcutaneous space of each mouse ($n = 5$). The sham group ($n = 4$), which served as a control, was subjected to the same surgery procedures but without film implantation. The incision was closed using interrupted sutures followed by standard combined postoperative analgesic regimen. After 4 weeks, the mice both in the implantation and sham groups were euthanized to collect blood, organs, and tissues for subsequent blood, elemental, and histological analyses.

To evaluate the distribution of Si resulting from film degradation, organs, including heart, spleen, kidney, brain, lung, and liver were collected and weighed, and then dissolved in 15 mL tubes (metal-free, Thermo Fisher Scientific) using solutions of 250 µL HNO_3 and 125 µL H_2O_2 to each heart, spleen, and lung sample and solutions of 500 µL HNO_3 and 125 µL H_2O_2 to each liver, kidney, and brain sample, which were kept in a water bath at 65 °C for 3 h until the organs were fully digested, and diluted with Millipore water to 5 or 10 mL after the solution cooled to room temperature. The solution was then analyzed by inductively coupled plasma optical emission spectrometry (iCAP 6500, Thermo Fisher Scientific). All measurements were performed simultaneously at three different wavelengths 212.412, 251.611, and 221.667 nm and the results presented here were obtained by averaging the values of these emission lines.

To assess the overall health of mice implanted with films, blood samples were collected and tested at the Veterinary Diagnostic Laboratory at University of Illinois. Blood was collected in collection tubes with K2-EDTA coatings and fully mixed with K2-EDTA to obtain the whole blood for CBC test. To obtain serum for blood chemistry tests, blood was collected in tubes without K2-EDTA coatings and centrifuged at 5000 rpm for 10 min after immersion in an ice bath for 5 min. The serum was transferred to a new tube using a pipette.

For histological studies, subcutaneous tissue and muscle were collected, fixed, and stored in formalin in 15 mL tubes (Thermo Fisher Scientific), followed by embedding in paraffin, sectioning, and staining with hematoxylin and eosin at the Mouse Histology and Phenotyping Laboratory at Northwestern University. These tissue samples were observed using bright-field microscopy (VS120, Olympus). The thickness of skin including dermis and hypodermis was blindly analyzed using unpaired two-tailed *t*-test, which showed no significant differences between implantation and sham groups.

In Vivo Water Barrier Performance of the Trilayer Materials: All procedures associated with the animal studies followed the Guide for the Care and Use of Laboratory Animals of the National Institutes of Health and approved by The Institutional Animal Care and Use Committee at Northwestern University (approval number: IS00024102).

Female mice (C57/BL6; age at the initiation of the treatment: 8–12 weeks; Charles River Laboratories) were anaesthetized using isoflurane gas (1–2% isoflurane in oxygen) in an anesthetizing chamber before the implantation surgery. After sterilizing by UV irradiation overnight, three LED devices that were encapsulated using the trilayer materials were implanted on the back of each mouse ($n = 3$). Mice in the control group ($n = 3$) were underwent the same surgery procedures but the implanted device lacked film encapsulation. The incision was closed using interrupted sutures followed by standard combined postoperative analgesic regimen. After a designated implantation period, the mice both in the implantation and the control groups were anaesthetized to collect data on resonant frequency of the implanted devices and LED illumination conditions. One out of three devices failed to illuminate LEDs due to a shift in frequency and the decrease in reflection coefficient of the device, indicating a limitation in the lifetime of encapsulation materials within mice.

Statistical Analysis: All results present as mean ± standard deviation with $n \geq 3$. The unpaired two-tailed *t*-test ($p < 0.05$) was used for statistical significance testing for histological analysis. The Kruskal–Wallis test was used for in vitro biocompatibility analysis. GraphPad Prism software was used to perform statistical analysis. ImageJ software was used to process the region of interest in images.

Supporting Information

Supporting Information is available from the Wiley Online Library or from the author.

Acknowledgements

Z.H., J.Z., H.G., and R.L. contributed equally to this work. This work utilized Northwestern University Micro/Nano Fabrication Facility (NUFAB), Electron Probe Instrumentation Center (EPIC), Keck Interdisciplinary Surface Science facility (Keck-II), Scanned Probe Imaging and Development (SPID) facility of Northwestern University's NUANCE Center, which received support from Soft and Hybrid Nanotechnology Experimental (SHyNE) Resource (NSF ECCS-2025633), the IIN, and Northwestern's MRSEC program (NSF DMR-1720139), and the Querrey-Simpson Institute for Bioelectronics. The authors thank M.S. Nayereh Ghoreishi-Haack and Dr. Elizabeth Dempsey for the help with the studies on CBC and blood chemistry and thank Dr. Rizaldy P. Scott and Sheila Mae B. Acar for tissue sectioning and staining. The authors thank Dr. Reiner Bleher for the discussion on the preparation of film implants for SEM characterization. The authors also thank M.Sc. Rebecca A. Sponenburg for the measurements of Si distribution in organs. J.Z. acknowledges the support from Science & Technology Commission of Shanghai Municipality (21ZR1409300 and 23160714000) and Open Research Fund of State Key Laboratory of Bioelectronics, Southeast University (SKLB2022-K09). R.L. acknowledges the support from the National Natural Science Foundation of China (Grant Nos. 12022209 and 12372067). Z.X. acknowledges the support from the National Natural Science Foundation of China (Grant No. 12072057), LiaoNing Revitalization Talents Program (Grant No. XLYC2007196), Dalian Outstanding Young Talents in Science and Technology (2021RJ06), and International Cooperation Fund Project of DBJI (Grant No. ICR2110). Y.H. acknowledges support from NSF (CMMI1635443).

Conflict of Interest

The authors declare no conflict of interest.

Data Availability Statement

The data that support the findings of this study are available from the corresponding author upon reasonable request.

Keywords

biofluid barriers, bioresorbable electronics, electronics packaging, silicon oxynitrides, transient electronics

Received: August 3, 2023
Revised: January 25, 2024
Published online: February 11, 2024

[1] T. Lei, M. Guan, J. Liu, H. C. Lin, R. Pfattner, L. Shaw, A. F. McGuire, T. C. Huang, L. L. Shao, K. T. Cheng, J. B. H. Tok, Z. N. Bao, *Proc. Natl. Acad. Sci. USA* **2017**, *114*, 5107.

[2] S. W. Hwang, H. Tao, D. H. Kim, H. Y. Cheng, J. K. Song, E. Rill, M. A. Brenckle, B. Panilaitis, S. M. Won, Y. S. Kim, Y. M. Song, K. J. Yu, A. Ameen, R. Li, Y. W. Su, M. M. Yang, D. L. Kaplan, M. R. Zakin, M. J. Slepian, Y. G. Huang, F. G. Omenetto, J. A. Rogers, *Science* **2012**, *337*, 1640.
[3] R. Li, L. Wang, D. Kong, L. Yin, *Bioact. Mater.* **2018**, *3*, 322.
[4] R. Singh, M. J. Bathaei, E. Istif, L. Beker, *Adv. Healthcare Mater.* **2020**, *9*, 2000790.
[5] J.-S. Shim, J. A. Rogers, S.-K. Kang, *Mater. Sci. Eng., R* **2021**, *145*, 100624.
[6] W. Bai, J. Shin, R. Fu, I. Kandela, D. Lu, X. Ni, Y. Park, Z. Liu, T. Hang, D. Wu, Y. Liu, C. R. Haney, I. Stepien, Q. Yang, J. Zhao, K. R. Nandoliya, H. Zhang, X. Sheng, L. Yin, K. MacRenaris, A. Brikha, F. Aird, M. Pezhouh, J. Hornick, W. Zhou, J. A. Rogers, *Nat. Biomed. Eng.* **2019**, *3*, 644.
[7] D. Lu, Y. Yan, Y. J. Deng, Q. S. Yang, J. Zhao, M. H. Seo, W. B. Bai, M. R. MacEwan, Y. G. Huang, W. Z. Ray, J. A. Rogers, *Adv. Funct. Mater.* **2020**, *30*, 2003754.
[8] C. M. Boutry, Y. Kaizawa, B. C. Schroeder, A. Chortos, A. Legrand, Z. Wang, J. Chang, P. Fox, Z. Bao, *Nat. Electron.* **2018**, *1*, 314.
[9] Y. S. Choi, R. T. Yin, A. Pfenniger, J. Koo, R. Avila, K. Benjamin Lee, S. W. Chen, G. Lee, G. Li, Y. Qiao, *Nat. Biotechnol.* **2021**, *39*, 1228.
[10] S.-W. Hwang, G. Park, H. Cheng, J.-K. Song, S.-K. Kang, L. Yin, J.-H. Kim, F. G. Omenetto, Y. Huang, K.-M. Lee, J. A. Rogers, *Adv. Mater.* **2014**, *26*, 1992.
[11] K. Liu, H. Tran, V. R. Feig, Z. Bao, *MRS Bull.* **2020**, *45*, 96.
[12] V. R. Feig, H. Tran, Z. Bao, *ACS Cent. Sci.* **2018**, *4*, 337.
[13] S. Mangaraj, A. Yadav, L. M. Bal, S. K. Dash, N. K. Mahanti, *J. Package Technol. Res.* **2019**, *3*, 77.
[14] J. L. Enming Song, J. A. Rogers, *APL Mater.* **2019**, *7*, 050902.
[15] M.-C. Choi, Y. Kim, C.-S. Ha, *Prog. Polym. Sci.* **2008**, *33*, 581.
[16] S. M. Won, J. Koo, K. E. Crawford, A. D. Mickle, Y. G. Xue, S. Min, L. A. McIlvried, Y. Yan, S. B. Kim, S. M. Lee, B. H. Kim, H. Jang, M. R. MacEwan, Y. G. Huang, R. W. Gereau, J. A. Rogers, *Adv. Funct. Mater.* **2018**, *28*, 1801819.
[17] M. Regert, J. Langlois, S. Colinart, *J. Chromatogr. A* **2005**, *1091*, 124.
[18] Y. S. Choi, J. Koo, Y. J. Lee, G. Lee, R. Avila, H. Ying, J. Reeder, L. Hambitzer, K. Im, J. Kim, K.-M. Lee, J. Cheng, Y. Huang, S.-K. Kang, J. A. Rogers, *Adv. Funct. Mater.* **2020**, *30*, 2000941.
[19] G. Li, Z. Ma, C. You, G. Huang, E. Song, R. Pan, H. Zhu, J. Xin, B. Xu, T. Lee, Z. An, Z. Di, Y. Mei, *Sci. Adv.* **2020**, *6*, 6511.
[20] G.-J. Ko, S. D. Han, J.-K. Kim, J. Zhu, W. B. Han, J. Chung, S. M. Yang, H. Cheng, D.-H. Kim, C.-Y. Kang, S.-W. Hwang, *NPG Asia Mater.* **2020**, *12*, 71.
[21] L. M. Jurkic, I. Cepanec, S. K. Pavelic, K. Pavelic, *Nutr. Metab.* **2013**, *10*, 2.
[22] E. M. Carlisle, *Nutr Rev* **1982**, *40*, 193.
[23] S.-K. Kang, S.-W. Hwang, H. Cheng, S. Yu, B. H. Kim, J.-H. Kim, Y. Huang, J. A. Rogers, *Adv. Funct. Mater.* **2014**, *24*, 4427.
[24] Y. C. Lin, Q. K. Le, L. W. Lai, R. M. Liao, M. S. Jeng, D. S. Liu, *Int. J. Eng. Technol. Innovation* **2012**, *2*, 184.
[25] M. Ohashi, S. Kanzaki, H. Tabata, *J. Am. Ceram. Soc.* **1991**, *74*, 109.
[26] H. Fang, J. N. Zhao, K. J. Yu, E. M. Song, A. B. Farimani, C. H. Chiang, X. Jin, Y. G. Xue, D. Xu, W. B. Du, K. J. Seo, Y. D. Zhong, Z. J. Yang, S. M. Won, G. H. Fang, S. W. Choi, S. Chaudhuri, Y. G. Huang, M. A. Alam, J. Viventi, N. R. Aluru, J. A. Rogers, *Proc. Natl. Acad. Sci. USA* **2016**, *113*, 11682.
[27] H. Guo, D. D'Andrea, J. Zhao, Y. Xu, Z. Qiao, L. E. Janes, N. K. Murthy, R. Li, Z. Xie, Z. Song, *Adv. Funct. Mater.* **2021**, *31*, 2102724.
[28] J. Koo, M. R. MacEwan, S. K. Kang, S. M. Won, M. Stephen, P. Gamble, Z. Q. Xie, Y. Yan, Y. Y. Chen, J. Shin, N. Birenbaum, S. J. Chung, S. B. Kim, J. Khalifeh, D. V. Harburg, K. Bean, M. Paskett, J. Kim, Z. S. Zohny, S. M. Lee, R. Y. Zhang, K. J. Luo, B. W. Ji, A. Banks, H. M. Lee, Y. G. Huang, W. Z. Ray, J. A. Rogers, *Nat. Med.* **2018**, *24*, 1830.
[29] G. Yao, L. Kang, C. Li, S. Chen, Q. Wang, J. Yang, Y. Long, J. Li, K. Zhao, W. Xu, *Proc. Natl. Acad. Sci. USA* **2021**, *118*, 2100772118.
[30] Y. Yang, M. Wu, A. Vázquez-Guardado, A. J. Wegener, J. G. Grajales-Reyes, Y. Deng, T. Wang, R. Avila, J. A. Moreno, S. Minkowicz, *Nat. Neurosci.* **2021**, *24*, 1035.
[31] H.-I. Lee, J.-B. Park, W. Xianyu, K. Kim, J. G. Chung, Y. K. Kyoung, S. Byun, W. Y. Yang, Y. Y. Park, S. M. Kim, *Sci. Rep.* **2017**, *7*, 1.
[32] H. Huang, K. J. Winchester, A. Suvorova, B. R. Lawn, Y. Liu, X. Z. Hu, J. M. Dell, L. Faraone, *Mater. Sci. Eng., A* **2006**, *435*, 453.
[33] M. Jozwik, P. Delobelle, C. Gorecki, A. Sabac, L. Nieradko, C. Meunier, F. Munnik, *Thin Solid Films* **2004**, *468*, 84.
[34] D. Galusková, M. Hnatko, D. Galusek, P. Šajgalík, *J. Am. Ceram. Soc.* **2011**, *94*, 3035.
[35] E. Laarz, B. V. Zhmud, L. Bergström, *J. Am. Ceram. Soc.* **2000**, *83*, 2394.
[36] E. Song, H. Fang, X. Jin, J. Zhao, C. Jiang, K. J. Yu, Y. Zhong, D. Xu, J. Li, G. Fang, H. Du, J. Zhang, J. M. Park, Y. Huang, M. A. Alam, Y. Mei, J. A. Rogers, *Adv. Electron. Mater.* **2017**, *3*, 1700077.
[37] E. Song, Y. K. Lee, R. Li, J. Li, X. Jin, K. J. Yu, Z. Xie, H. Fang, Y. Zhong, H. Du, J. Zhang, G. Fang, Y. Kim, Y. Yoon, M. A. Alam, Y. Mei, Y. Huang, J. A. Rogers, *Adv. Funct. Mater.* **2018**, *28*, 1702284.
[38] E. Song, R. Li, X. Jin, H. Du, Y. Huang, J. Zhang, Y. Xia, H. Fang, Y. K. Lee, K. J. Yu, J.-K. Chang, Y. Mei, M. A. Alam, Y. Huang, J. A. Rogers, *ACS Nano* **2018**, *12*, 10317.
[39] Y.-H. Kim, E. Lee, J. G. Um, M. Mativenga, J. Jang, *Sci. Rep.* **2016**, *6*, 25734.
[40] Z. Gan, C. Wang, Z. Chen, *Surfaces* **2018**, *1*, 59.